The Astrophysical Journal, 755:62 (13pp), 2012 August 10 doi:10.1088/0004-637X/755/1/62

A NEW CODE FOR NONLINEAR FORCE-FREE FIELD EXTRAPOLATION OF THE GLOBAL CORONA

Chaowei Jiang, Xueshang Feng, and Changqing Xiang
SIGMA Weather Group, State Key Laboratory for Space Weather, Center for Space Science and Applied Research, Chinese Academy of Sciences, Beijing 100190, China; cwjiang@spaceweather.ac.cn
Received 2012 April 12; accepted 2012 June 6; published 2012 July 26

ABSTRACT

Reliable measurements of the solar magnetic field are still restricted to the photosphere, and our present knowledge of the three-dimensional coronal magnetic field is largely based on extrapolations from photospheric magnetograms using physical models, e.g., the nonlinear force-free field (NLFFF) model that is usually adopted. Most of the currently available NLFFF codes have been developed with computational volume such as a Cartesian box or a spherical wedge, while a global full-sphere extrapolation is still under development. A high-performance global extrapolation code is in particular urgently needed considering that the *Solar Dynamics Observatory* can provide a full-disk magnetogram with resolution up to 4096 × 4096. In this work, we present a new parallelized code for global NLFFF extrapolation with the photosphere magnetogram as input. The method is based on the magnetohydrodynamics relaxation approach, the CESE–MHD numerical scheme, and a Yin–Yang spherical grid that is used to overcome the polar problems of the standard spherical grid. The code is validated by two full-sphere force-free solutions from Low & Lou's semi-analytic force-free field model. The code shows high accuracy and fast convergence, and can be ready for future practical application if combined with an adaptive mesh refinement technique.

Key words: magnetic fields – magnetohydrodynamics (MHD) – methods: numerical – Sun: corona

Online-only material: color figures

1. INTRODUCTION

The magnetic field holds a central position within solar research such as sunspots and coronal loops, prominences, solar flares, solar wind, and coronal mass ejections (CMEs). However, a routinely direct measurement of the solar magnetic field on which we can rely is restricted to the solar surface, i.e., the photosphere, in spite of the works that have been done to measure the coronal fields using the radio and infrared wave bands (Gary & Hurford 1994; Lin et al. 2004). This is extremely unfortunate since the magnetic field plays a comparatively minor role in the photosphere but completely dominates proceedings in the corona (Solanki et al. 2006). Up to the present, our knowledge of the three-dimensional (3D) coronal magnetic field has been largely based on extrapolations from photospheric magnetograms using physical models. For the low corona, one model assuming that the corona is free of Lorentz force ($\mathbf{J} \times \mathbf{B} = \mathbf{0}$, where $\mathbf{J}$ is the current and $\mathbf{B}$ is the magnetic field) is justified by a rather small plasma β (the ratio of gas pressure to magnetic pressure) and a quasi-static state. The force-free assumption involves an intrinsically nonlinear equation $(\nabla \times \mathbf{B}) \times \mathbf{B} = \mathbf{0}$ that is rather difficult to solve if based on boundary information alone, and various computing codes have been proposed to solve this equation numerically for nonlinear force-free field (NLFFF) extrapolations (e.g., see review papers by Amari et al. 1997; McClymont et al. 1997; Schrijver et al. 2006; Metcalf et al. 2008; Wiegelmann 2008; DeRosa et al. 2009).

Most of the currently available NLFFF codes are developed in Cartesian coordinates. Thus, the extrapolations are limited to relatively local and small areas, e.g., a single active region (AR) without any relationship to other ARs. However, ARs usually cannot be isolated since they interact with the neighboring ARs or overlying large-scale fields. Observations of moving plasma connecting several separated ARs by the *Solar and Heliospheric Observatory* (*SOHO*) Extreme Ultraviolet Imaging Telescope reveal the connections between ARs (e.g., Wang et al. 2001). Also, the activities in the chromosphere and corona often spread over several ARs, such as filament bursts recorded in Hα images and CMEs observed by *SOHO* Large Angle and Spectrometric Coronagraphs. Even for a single AR, the fields of view in a Cartesian box are often too small to properly characterize the entire relevant current system (DeRosa et al. 2009). To study the connectivity between multi-ARs and extrapolate in a larger field of view, it is necessary to take into account the curvature of the Sun's surface by extrapolation in spherical geometry partly or even entirely, i.e., including the global corona (Wiegelmann 2007; Tadesse et al. 2011, 2012). Moreover, a global NLFFF extrapolation can avoid any lateral artificial boundaries that cause issues in Cartesian codes. Global non-potential extrapolations are urgently needed considering that high-resolution, full-disk vector magnetograms will be soon available from the *Solar Dynamics Observatory* (*SDO*). Another motivation comes from the developing of global MHD models for the solar corona and solar wind. Up to the present, the global MHD models have been based only on the line-of-sight (LoS) magnetogram, using the global potential extrapolation to initialize the computation (e.g., Feng et al. 2010). These models will be challenged by the full-sphere vector magnetogram, which needs a global non-potential extrapolation.

Over the past few years, several global NLFFF extrapolation methods have been developed, but they are still in their infancy and many issues need to be resolved. For example, He & Wang (2006) validated the boundary-integral-equation method (Yan & Li 2006) for extrapolation above a full sphere using simple models of Low & Lou (1990), while application to more complex extrapolations needs further development. Wiegelmann (2007) and Tadesse et al. (2009) extended their optimization code to spherical coordinates including those for both partial and full spheres, but the convergence speed is proved to be rather slow

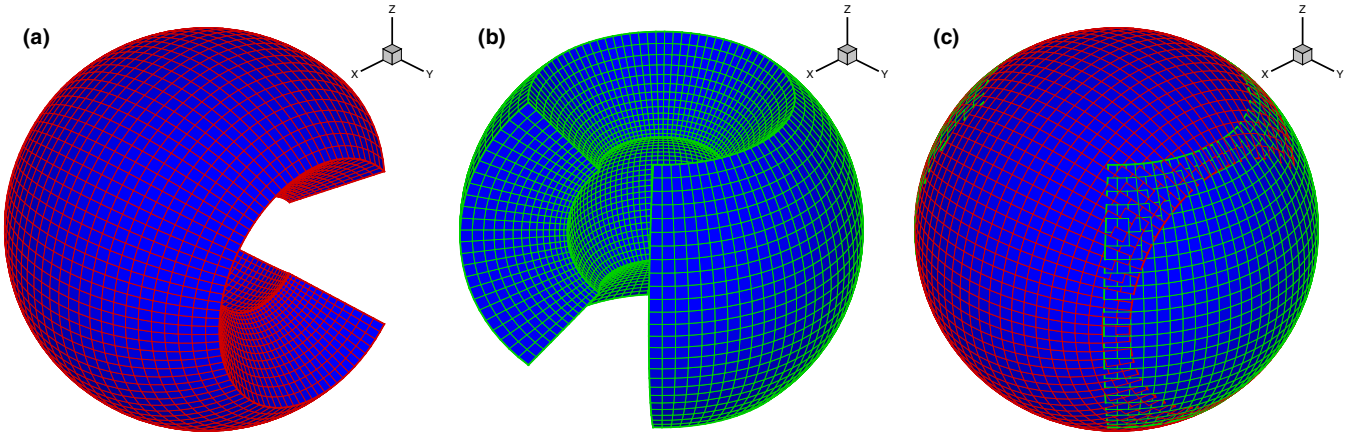

Figure 1. Yin–Yang grids: the component grids (a) Yin and (b) Yang, and (c) the overlapping grid.
(A color version of this figure is available in the online journal.)

if polar regions are included in the computation (Wiegelmann 2007). A flux rope insertion method based on magnetofriction was also developed by van Ballegooijen (2004) for constructing NLFFFs in spherical coordinates (e.g., see its applications by Bobra et al. 2008; Su et al. 2009a, 2009b; Savcheva & van Ballegooijen 2009), but the same problem as in Wiegelmann (2007) may be encountered if the code is extended to contain the whole sphere. Very recently, Contopoulos et al. (2011) presented a new force-free electrodynamics method for the global coronal field extrapolation; however, the solution is not unique since it is only prescribed by the radial magnetogram.

Among the existing problems, choosing a suitable grid system is in particular critical for the implementation of any global models (not only the global force-free extrapolation) with the lower boundary as the full solar surface. Naturally, one can use the spherical grid, i.e., with grid lines defined by coordinates (r, θ, ϕ). However, the simplicity of a standard-spherical coordinate grid is destroyed by the problem of grid convergence and grid singularity at both poles (Usmanov 1996; Kageyama & Sato 2004; Feng et al. 2010). These problems severely restrict the converge speed of the full-sphere optimization code as reported by Wiegelmann (2007). Although the singularity problem can be partially resolved by excluding a small high-latitude cone, e.g., restricting the latitude within $10^\circ \leqslant \theta \leqslant 170^\circ$, it inescapably disconnects the field lines crossing over the polar region. To avoid these problems, Contopoulos et al. (2011) simply use the Cartesian grid to implement their method by taking a cubic Cartesian box to contain the whole region with the solar sphere cut out. However, the Cartesian grid cannot characterize precisely the Sun's sphere surface, since the solar sphere nowhere coincides with any grid points. Thus, the corresponding boundary conditions are hard to prescribe. On the other hand, the unstructured grid has been used frequently in global MHD models (Tanaka 1994; Feng et al. 2007; Nakamizo et al. 2009) and can possibly be introduced into NLFFF extrapolation, but it has high costs in mesh generation and management and is not suitable for solvers based on numerical difference (though it may be suitable for a finite element solver, e.g., the FEMQ code developed by Amari et al. 2006). Moreover, on the unstructured grid, it is difficult to implement the technique of parallelized-adaptive mesh refinement (AMR), which is an attractive tool for resolving the contradiction between the computational demand for extrapolating high-resolution/large field-of-view magnetograms and the computational resource limitations. A promising solution to the above problems is the use of an overlapping spherical grid, e.g., the several types of overlapping spherical grids proposed by Usmanov (1996), Kageyama & Sato (2004), Henshaw & Schwendeman (2008), and Feng et al. (2010). In principle, one can use a set of low-latitude partial-sphere grids to cover the full sphere with some patches overlapped. Certainly, in such an overlapping grid system, there are no pole problems; meanwhile, the grid management is easy. If the component grids are carefully chosen, the overlapping patches can be minimized and only add a very small numerical overhead to the computation for data communications between the component grids. Among the overlapping grids for composing the full sphere, a so-called Yin–Yang grid (Kageyama & Sato 2004) is a most elegant configuration with only two identical components and an overlapping region smaller than 7% of the full sphere (see Figure 1).

Our previous work (Jiang et al. 2011; Jiang & Feng 2012a) was devoted to a new implementation of the MHD relaxation approach for NLFFF extrapolation based on the CESE numerical scheme (spacetime conservation-element and solution-element scheme). We have introduced a new set of magneto-frictional-like equations with the AMR and a multigrid-like strategy for accelerating the computation and improving its convergence. The good performance and high accuracy of the code has been demonstrated through detailed comparisons with previous work by Schrijver et al. (2006) and Metcalf et al. (2008) based on several NLFFF benchmark tests, although it remains to be seen how well this method will work with real solar data. The success of the CESE–MHD–NLFFF code encourages us to extend it to spherical geometry and ultimately realize a fast and accurate way for the global non-potential extrapolation of the high-resolution full-disk magnetograms from *SDO*. In this paper, we take the first step by developing a new code for global NLFFF extrapolation using the CESE–MHD–NLFFF method on the Yin–Yang grid. This code is assumed to be applied to force-free vector magnetograms, i.e., with the uncertainties and inconsistencies removed by some kind of preprocessing approach, e.g., that proposed by Wiegelmann et al. (2006). This is important considering that NLFFF codes generally have failed to extrapolate a satisfactory force-free field when applied to the non-force-free magnetogram (Metcalf et al. 2008), which is usually the case with observed data.

The remainder of the paper is organized as follows: In Section 2, we give the model equations and the numerical

method including a curvilinear-version CESE–MHD scheme and its implementation in the Yin–Yang grid. In Section 3, we set up two semi-analytic test cases of the full-sphere NLFFF solution proposed by Low & Lou (1990). The extrapolation results and qualitative and quantitative comparisons are presented in Section 4. Finally, we draw conclusions and give some outlooks for future work in Section 5.

2. THE METHOD

2.1. Model Equations

The basic idea of using the MHD relaxation approach to solve the force-free field is to use some kind of fictitious dissipation to drive the MHD system to an equilibrium in which all the forces can be neglected if compared to the Lorentz force and the boundary vector map is satisfied. In our previous work for NLFFF extrapolation (Jiang & Feng 2012a), a magnetic splitting form of magneto-frictional model equations was introduced as

$$\begin{aligned} \frac{\partial \rho \mathbf{v}}{\partial t} &= (\nabla \times \mathbf{B}_1) \times \mathbf{B} - \nu \rho \mathbf{v}, \\ \frac{\partial \mathbf{B}_1}{\partial t} &= \nabla \times (\mathbf{v} \times \mathbf{B}) + \nabla(\mu \nabla \cdot \mathbf{B}_1) - \mathbf{v} \nabla \cdot \mathbf{B}_1, \\ \frac{\partial \mathbf{B}_0}{\partial t} &= \mathbf{0}, \nabla \times \mathbf{B}_0 = \mathbf{0}, \nabla \cdot \mathbf{B}_0 = 0, \\ \rho &= |\mathbf{B}|^2 + \rho_0, \ \mathbf{B} = \mathbf{B}_0 + \mathbf{B}_1. \end{aligned} \tag{1}$$

In the above equation system, $\mathbf{B}_0$ is a potential field matching the normal component of the magnetogram, $\mathbf{B}_1$ is the deviation between the potential field $\mathbf{B}_0$ and the force-free field $\mathbf{B}$ to be solved, ν is the frictional coefficient, and μ is a numerical diffusive speed of the magnetic monopole; ρ_0 is a necessary small value (e.g., $\rho_0 = 0.01$) to deal with the very weak field associated with the magnetic null. The values for parameters ν and μ are, respectively, given by $\nu = \Delta t/\Delta x^2$ and $\mu = 0.4\Delta x^2/\Delta t$, according to the time step Δt and local grid size Δx. The merits of using the above equations include the following:

1. Retaining explicitly the time-dependent form of the momentum equation[1] makes the magneto-frictional equation system able to be handled by the modern computational fluid dynamics or MHD solver designed for the standard partial-differential-equation system like

$$\frac{\partial \mathbf{U}}{\partial t} + \frac{\partial \mathbf{F}(\mathbf{U})}{\partial x} + \frac{\partial \mathbf{G}(\mathbf{U})}{\partial y} + \frac{\partial \mathbf{H}(\mathbf{U})}{\partial z} = \mathbf{S}. \tag{2}$$

2. Numerically, accuracy can be gained only for solving the deviation field $\mathbf{B}_1$ by dividing the total magnetic field $\mathbf{B}$ into two parts ($\mathbf{B} = \mathbf{B}_0 + \mathbf{B}_1$) (Tanaka 1994). Also, such a splitting has a physical meaning (Priest & Forbes 2002): Potential component $\mathbf{B}_0$ arises from photospheric or sub-photospheric currents and can be regarded as invariant during a flare, whereas the non-potential component $\mathbf{B}_1$ arises from large-scale coronal currents (above the photosphere) and is the source of the flare energy.
3. Any numerical magnetic monopoles $\nabla \cdot \mathbf{B}_1$ can be rapidly convected away with the plasma by term $-\mathbf{v}\nabla \cdot \mathbf{B}_1$ and effectively diffused out by term $\nabla(\mu \nabla \cdot \mathbf{B}_1)$.
4. Setting a pseudo-plasma density $\rho \propto |\mathbf{B}|^2$ can equalize the Alfvén speed of the whole domain and thus accelerate the relaxation in the weak field regions.

[1] This is unlike the standard magneto-frictional method in which the momentum equation is simplified as $\nu \mathbf{v} = \mathbf{J} \times \mathbf{B}$. Although the standard magneto-frictional method is simpler since only the induction equation $\partial \mathbf{B}/\partial t = \nabla \times (\mathbf{v} \times \mathbf{B}) = \nabla \times ((\mathbf{J} \times \mathbf{B}/\nu) \times \mathbf{B})$ is needed to be solved, this equation cannot be written in the form of Equation (2).

2.2. Numerical Implementation

To solve the model Equation (1) in spherical geometry, we employ a curvilinear version of the CESE–MHD solver proposed by Jiang et al. (2010). In this method, the governing equations written as Equation (2) are transformed from the physical space (x, y, z) into a reference space (ξ, η, ζ) whose mapping is explicitly known as $x = x(\xi, \eta, \zeta)$; $y = y(\xi, \eta, \zeta)$; $z = z(\xi, \eta, \zeta)$. The transformed equations are

$$\frac{\partial \hat{\mathbf{U}}}{\partial t} + \frac{\partial \hat{\mathbf{F}}}{\partial \xi} + \frac{\partial \hat{\mathbf{G}}}{\partial \eta} + \frac{\partial \hat{\mathbf{H}}}{\partial \zeta} = \hat{\mathbf{S}}, \tag{3}$$

where

$$\begin{cases} \hat{\mathbf{U}} = J\mathbf{U}, \\ \hat{\mathbf{F}} = J(\mathbf{F}\xi_x + \mathbf{G}\xi_y + \mathbf{H}\xi_z), \\ \hat{\mathbf{G}} = J(\mathbf{F}\eta_x + \mathbf{G}\eta_y + \mathbf{H}\eta_z), \\ \hat{\mathbf{H}} = J(\mathbf{F}\zeta_x + \mathbf{G}\zeta_y + \mathbf{H}\zeta_z), \\ \hat{\mathbf{S}} = J\mathbf{S}, \end{cases} \tag{4}$$

and J is the determinant of Jacobian matrix $\mathbf{J}$ for the mapping, i.e.,

$$\mathbf{J} = \frac{\partial(x, y, z)}{\partial(\xi, \eta, \zeta)} = \begin{pmatrix} x_\xi & x_\eta & x_\zeta \\ y_\xi & y_\eta & y_\zeta \\ z_\xi & z_\eta & z_\zeta \end{pmatrix}. \tag{5}$$

Based on this transformation, the basic idea is to map the spherical geometry of physical space to a simple rectangular grid of the reference space, in which we can use the Cartesian CESE–MHD method to solve the transformed equations with very simple rectangular-uniform mesh. For detailed descriptions of the CESE–MHD method and its curvilinear version, please refer to Jiang et al. (2010) and Feng et al. (2012).

To overcome the grid-singularity problem at both poles of the standard spherical coordinates, we use the Yin–Yang grid. As a type of overlapping grid, the Yin–Yang grid is synthesized by two identical component grids in a complementary way to cover an entire spherical surface with partial overlap on their boundaries (see Figure 1). Each component grid is a low latitude part of the latitude–longitude grid without the pole. Therefore, the grid spacing on the sphere surface is quasi-uniform and the metric tensors (i.e., the matrix elements in Equation (5)) are simple and analytically known (Kageyama & Sato 2004). In Figure 1, one component grid, say the "Yin" grid, is defined in the spherical coordinates by

$$|\theta - \pi/2| \leqslant \pi/4 + \delta; \ |\phi - \pi| \leqslant 3\pi/4 + \delta, \tag{6}$$

where $\delta = 1.5\Delta\theta$ is a small buffer to minimize the required overlap. The other component grid, the "Yang" grid, is defined by the same rule of Equation (6) but in another coordinate system that is rotated from the Yin's. The relation between Yin and Yang coordinates is denoted in Cartesian coordinates of each one by $(x_e, y_e, z_e) = (-x_n, z_n, y_n)$, where (x_n, y_n, z_n) is Yin's Cartesian coordinates and (x_e, y_e, z_e) is Yang's.

We then map the Yin and Yang component grids to rectangular grids by defining two mapping equations

$$\text{Yin}\begin{cases} x = e^{\xi}\sin\theta\cos\phi \\ y = e^{\xi}\sin\theta\sin\phi \\ z = e^{\xi}\cos\theta \end{cases} \quad (7)$$

and

$$\text{Yang}\begin{cases} x = -e^{\xi}\sin\theta\cos\phi \\ y = e^{\xi}\cos\theta \\ z = e^{\xi}\sin\theta\sin\phi, \end{cases} \quad (8)$$

where (ξ, θ, ϕ) are the coordinates of the reference space with the rectangular-uniform mesh used ($\Delta\xi = \Delta\theta = \Delta\phi$). In this definition, we have

$$\Delta r = e^{\xi+\Delta\xi} - e^{\xi} = e^{\xi}(e^{\Delta\xi} - 1) \approx r\Delta\xi = r\Delta\theta, \quad (9)$$

which means that the cells are close to regular cubes in physical space, especially at low latitudes.

The grid extent in ξ is $\xi \in [0, \ln 10]$, i.e., the outer boundary is set at $r = 10R_S$ (solar radius). The initial condition is specified by simply setting $\mathbf{B}_1 = \mathbf{0}$ and $\mathbf{v} = \mathbf{0}$. The constant part $\mathbf{B}_0$ is obtained by a fast potential field solver which is developed by a combination of the spectral and the finite-difference methods (Jiang & Feng 2012b). The lower boundary condition is given by the vector magnetogram, while the outer boundary is fixed with zero values of $\mathbf{B}_1$ and $\mathbf{v}$. In the following test cases, we focus on the field extrapolation in $r \in [1, 2]R_S$, and the objective of setting the outer boundary far beyond the extrapolation volume is to minimize the boundary effect.

On the boundaries where grids overlap, solution values on one component grid are determined by interpolation from the other. We use explicit interpolation for simplicity and efficiency in parallel computation, and the grid buffer δ is suitably chosen for enough overlap area to perform such interpolation (see Figure 1). In the reference space, standard tensor-product Lagrange interpolation (Isaacson & Keller 1966) is used. For instance (see Figure 2 for details), the interpolation of value f at the point $M(\xi_M, \eta_M, \zeta_M)$ in the reference space is computed by $f(M) = \sum_{k=0}^{2}\sum_{j=0}^{2}\sum_{i=0}^{2} f(i, j, k)P_i^M(\xi)P_j^M(\eta)P_k^M(\zeta)$, where $P_j^M(x)$ is the Lagrange interpolating polynomial $P_j^M(x) = \prod_{k=0,k\neq j}^{2}(x_M - x_k/x_j - x_k)$ with x being ξ, η or ζ. Note that the interpolation accuracy is of three orders, which is higher than the CESE solver by one order. Thus, the discretization accuracy in the overlapping region will not be reduced by the interpolation. Finally, to realize the parallelization on these bi-component grids, each component grid is divided into small blocks consisting of $8 \times 8 \times 8$ cells with guard cells (one layer of ghost cells for convenience of communication between blocks), which are distributed evenly among the processors. The message-passing-interface library is employed for data communications between the processors. The interpolation of the overlapping boundaries is dealt with in a similar way to that for the intra-grid guard-cell filling, and both operations are arranged to be done simultaneously. The load balancing is also considered carefully among all the processors to further improve the parallel scaling.

3. TEST CASE

The NLFFF model derived by Low & Lou (1990) has served as a standard benchmark for many extrapolation codes

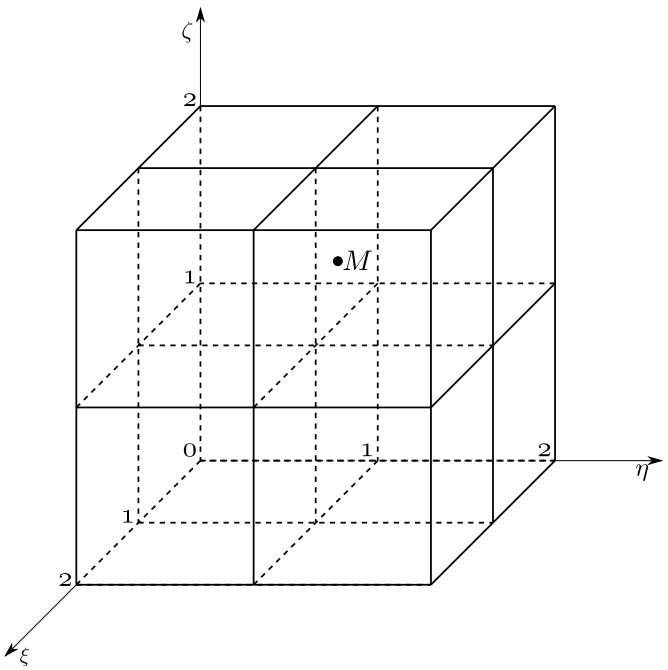

Figure 2. Interpolation of point M in the reference space: If M represents a mesh point on the overlapping boundary, for example, of the Yin grid, then the twenty-seven (3^3) nodes denote Yang's inner mesh points that are closest to M.

(Wheatland et al. 2000; Amari et al. 2006; Schrijver et al. 2006; Valori et al. 2007; He & Wang 2008; Jiang et al. 2011). The fields of this model are basically axially symmetric and can be represented by a second-order ordinary differential equation of $P(\mu)$ derived in spherical coordinates

$$(1-\mu^2)\frac{d^2P}{d\mu^2} + n(n+1)P + a^2\frac{1+n}{n}P^{1+2/n} = 0, \quad (10)$$

where n and a are constants and $\mu = \cos\theta$. With boundary conditions of $P = 0$ at $\mu = -1, 1$, the solution P of Equation (10) is uniquely determined by two eigenvalues, n and its number of nodes m (Low & Lou 1990; Amari et al. 2006). The magnetic fields are then given by

$$B_r = \frac{1}{r^2\sin\theta}\frac{\partial A}{\partial\theta}, B_\theta = -\frac{1}{r\sin\theta}\frac{\partial A}{\partial r}, B_\phi = \frac{1}{r\sin\theta}Q, \quad (11)$$

where $A = P(\mu)/r^n$ and $Q = aA^{1+1/n}$. The fields are axisymmetric in spherical coordinates (i.e., invariant in the ϕ direction) with a point source at the origin. To avoid such obvious symmetry in the full-3D extrapolation test, we locate the point source with $0.3R_S$ offset to the center of the computational volume and deviate the axis of symmetry with the z-axis by $\Phi = \pi/10$ (the length unit of the above equations is the solar radius R_S). We present two test cases with eigenvalues of $n = 1, m = 1$ (hereafter referred to as CASE LL1) and $n = 3, m = 1$ (CASE LL2), respectively. Both cases are performed with the same resolution of 90×180 grids in the θ–ϕ plane and $r \in [1, 2]R_S$. The synoptic maps of the field and the force-free parameter α at the bottom of the solutions are shown in Figures 3 and 4, and the 3D field lines are shown in panels (a) of Figures 5 and 6. It should be remarked that these magnetograms do not represent the real magnetic distributions of the photosphere but only are to be used for the purpose of testing our code. As can be seen, the α distribution of CASE LL2 is more inhomogeneous than that of CASE LL1, which means

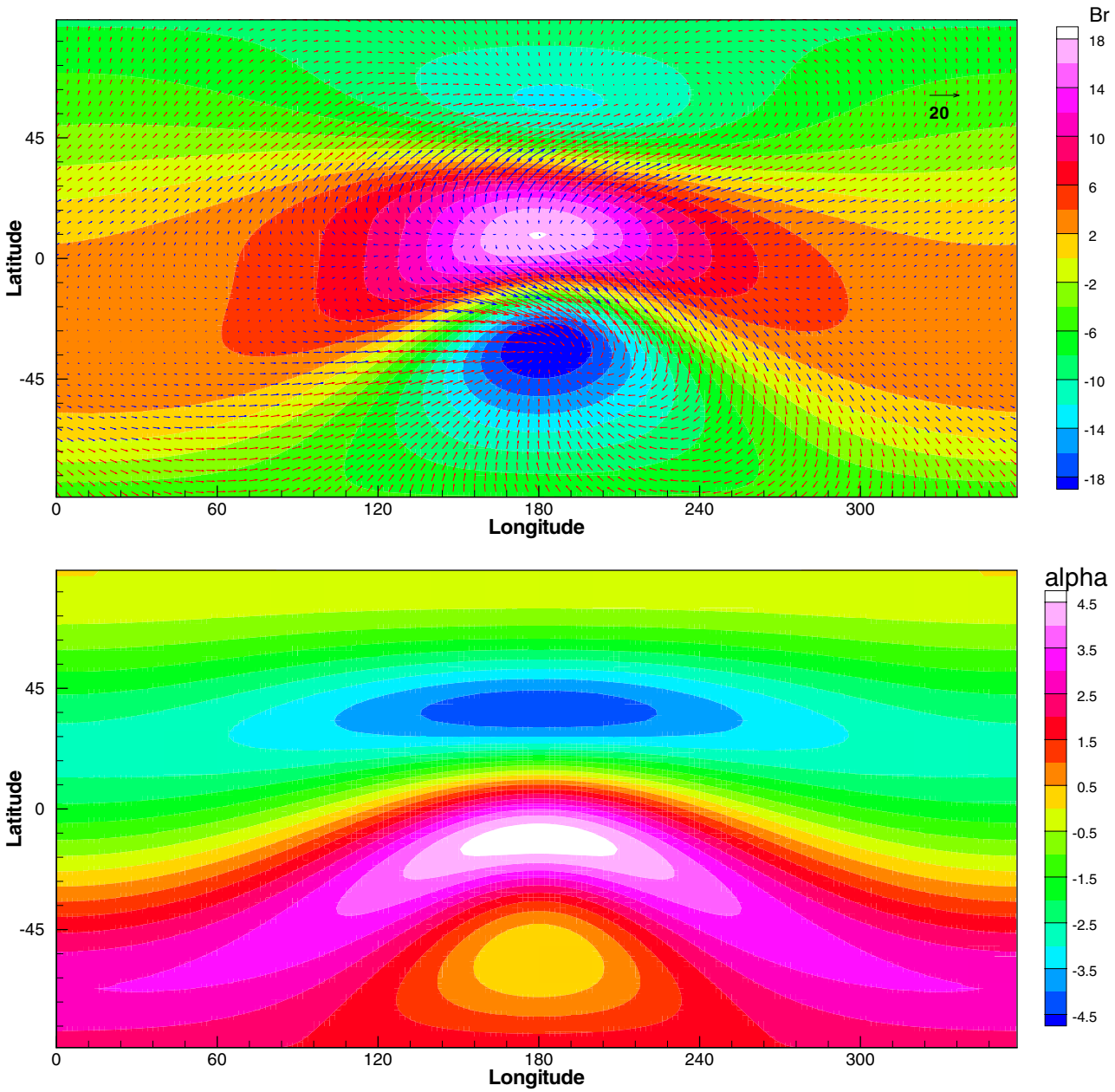

Figure 3. Vector map (upper) and α distribution (bottom) of CASE LL1. In the vector map the contours represent B_r, and the tangential field (B_ϕ, B_θ) is shown by the vectors with blue color in the positive B_r region and with red color in the negative B_r region.

(A color version of this figure is available in the online journal.)

that CASE LL2 is more nonlinear. We note that CASE LL1 is very similar to test cases used by Wiegelmann (2007) and Tadesse et al. (2009), while CASE LL2 is more difficult than tests in their works.

Before inputting the vector maps in the NLFFF code, we made some consistency checks for the maps. If a vector map is used for a force-free extrapolation, some necessary conditions have to be fulfilled (Aly 1989; Sakurai 1989; Tadesse et al. 2009). For clarification we repeat here these conditions from Tadesse (2011) where a detailed derivation of the condition formula is given. First, the net magnetic flux must be in balance, i.e.,

$$\int_S B_r \, ds = 0, \tag{12}$$

where S represents the whole sphere. Second, the total force on the boundary has to vanish, which can be expressed in spherical coordinates as

$$\begin{aligned}
\mathcal{F}_1 &= \int_S \Big[\frac{1}{2}(B_\theta^2 + B_\phi^2 - B_r^2)\sin\theta\cos\phi \\
&\quad - B_r B_\theta \cos\theta\cos\phi + B_r B_\phi \sin\phi\Big]\, ds = 0; \\
\mathcal{F}_2 &= \int_S \Big[\frac{1}{2}(B_\theta^2 + B_\phi^2 - B_r^2)\sin\theta\sin\phi \\
&\quad - B_r B_\theta \cos\theta\sin\phi - B_r B_\phi \cos\phi\Big]\, ds = 0; \\
\mathcal{F}_3 &= \int_S \Big[\frac{1}{2}(B_\theta^2 + B_\phi^2 - B_r^2)\cos\theta + B_r B_\theta \sin\theta\Big]\, ds = 0.
\end{aligned} \tag{13}$$

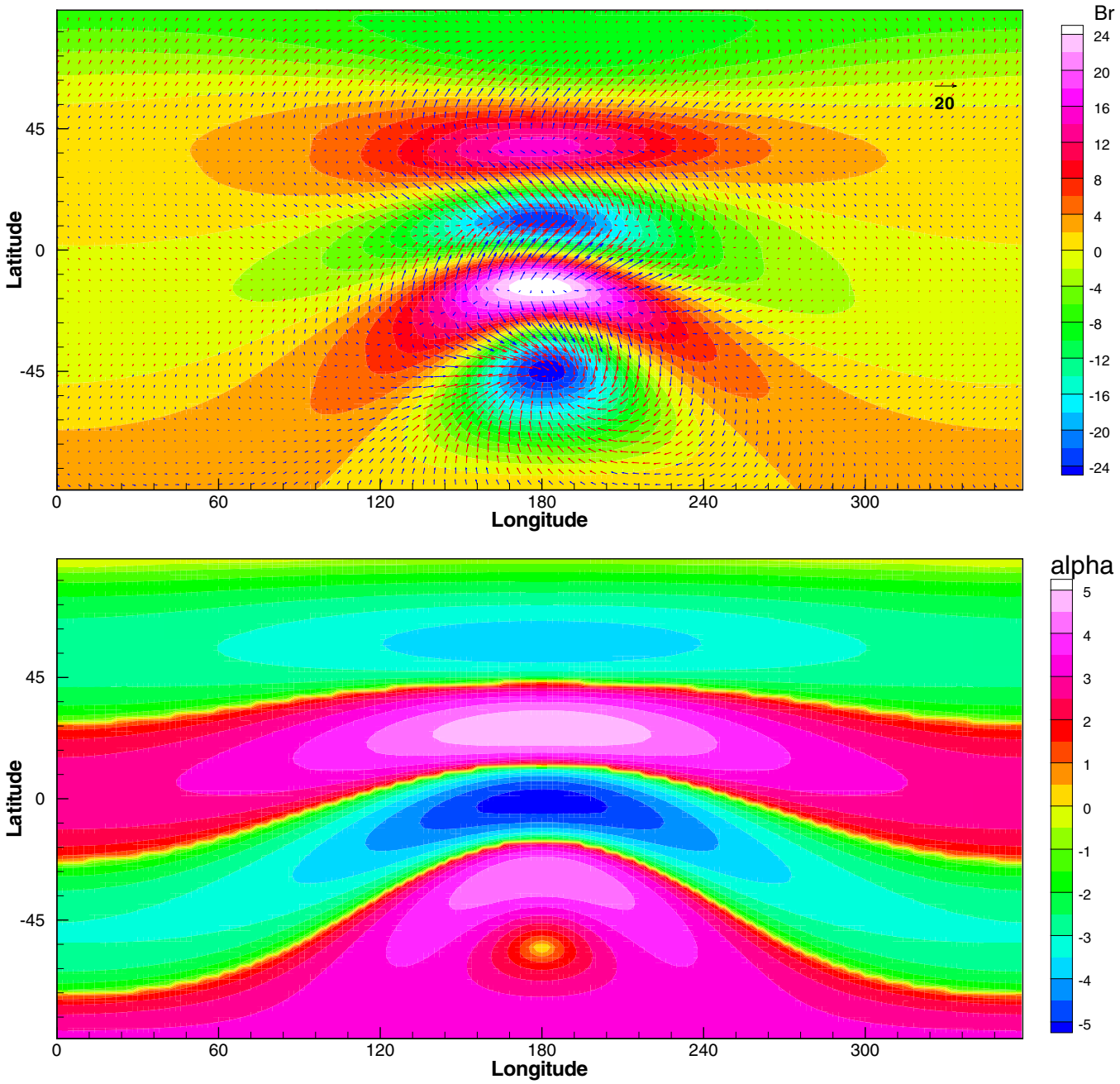

Figure 4. Same as Figure 3 but for CASE LL2.
(A color version of this figure is available in the online journal.)

Third, the total torque on the boundary vanishes, i.e.,

$$\mathcal{T}_1 = \int_S B_r(B_\phi \cos\theta \cos\phi + B_\theta \sin\phi)\, ds = 0;$$
$$\mathcal{T}_2 = \int_S B_r(B_\phi \cos\theta \sin\phi - B_\theta \cos\phi)\, ds = 0;$$
$$\mathcal{T}_3 = \int_S B_r B_\phi \sin\theta\, ds = 0. \quad (14)$$

To quantify the quality of the synthetic full-disk magnetograms with respect to the above criteria, we compute three parameters, i.e., the flux balance parameter

$$\epsilon_{\rm flux} = \frac{\int_S B_r\, ds}{\int_S |B_r|\, ds}, \quad (15)$$

the force balance parameter

$$\epsilon_{\rm force} = \frac{|\mathcal{F}_1| + |\mathcal{F}_2| + |\mathcal{F}_3|}{E_B}, \quad (16)$$

and the torque balance parameter

$$\epsilon_{\rm torque} = \frac{|\mathcal{T}_1| + |\mathcal{T}_2| + |\mathcal{T}_3|}{E_B}, \quad (17)$$

where $E_B = \int_S (B_r^2 + B_\theta^2 + B_\phi^2)\, ds$. For the above cases, the three parameters are $(-7.117 \times 10^{-4}, 1.181 \times 10^{-4}, 6.313 \times 10^{-6})$ and $(-1.028 \times 10^{-3}, 5.458 \times 10^{-4}, 7.379 \times 10^{-5})$, respectively, which shows that these maps are ideally consistent with the force-free model.

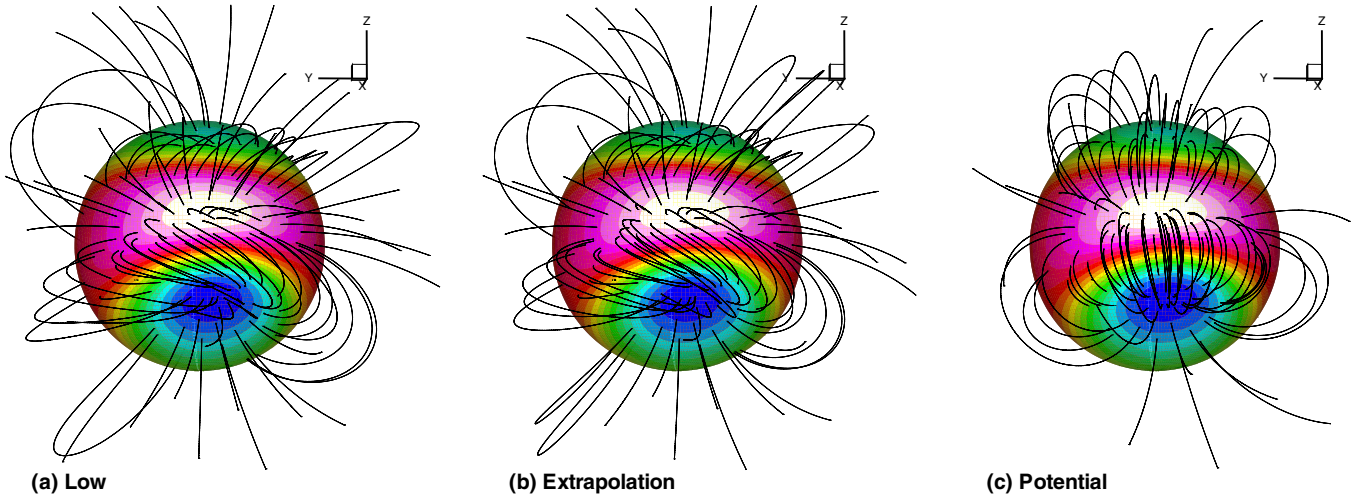

Figure 5. CASE LL1: 3D magnetic field lines with contour of B_r on the photosphere surface—(a) Low & Lou's solution; (b) the extrapolation result; and (c) the initial potential field.

(A color version of this figure is available in the online journal.)

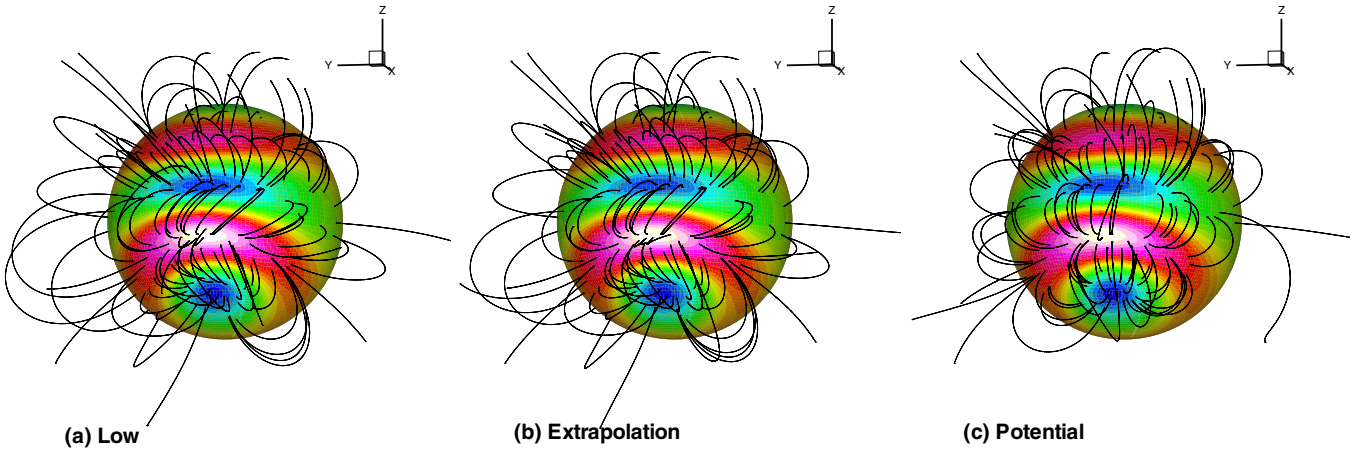

Figure 6. Same as Figure 5 but for CASE LL2.

(A color version of this figure is available in the online journal.)

4. RESULTS

In this section, we present the results of extrapolation and compare them with their original solutions qualitatively and quantitatively. As usual, the quantitative comparison is performed by computing a suite of metrics (also referred to as figures of merit), which are listed as follows:

1. the vector correlation $C_{\rm vec}$

$$C_{\rm vec} \equiv \sum_i \mathbf{B}_i \cdot \mathbf{b}_i \Big/ \left(\sum_i |\mathbf{B}_i|^2 \sum_i |\mathbf{b}_i|^2 \right); \quad (18)$$

2. the Cauchy–Schwarz inequality $C_{\rm CS}$

$$C_{\rm CS} \equiv \frac{1}{M} \sum_i \frac{\mathbf{B}_i \cdot \mathbf{b}_i}{|\mathbf{B}_i||\mathbf{b}_i|}; \quad (19)$$

3. the normalized and mean vector error $E'_{\rm n}$, $E'_{\rm m}$

$$E_{\rm n} \equiv \sum_i |\mathbf{b}_i - \mathbf{B}_i| \Big/ \sum_i |\mathbf{B}_i|; \; E'_{\rm n} = 1 - E_{\rm n}, \quad (20)$$

$$E_{\rm m} \equiv \frac{1}{M} \sum_i \frac{|\mathbf{B}_i - \mathbf{b}_i|}{|\mathbf{B}_i|}; \; E'_{\rm m} = 1 - E_{\rm m}; \text{ and} \quad (21)$$

4. the magnetic energy ratio ϵ

$$\epsilon = \frac{\sum_i |\mathbf{b}_i|^2}{\sum_i |\mathbf{B}_i|^2}; \quad (22)$$

where $\mathbf{B}_i$ and $\mathbf{b}_i$ denote the Low & Lou solution and the extrapolated field, respectively, i denotes the indices of the grid points, and M is the total number of grid points involved. It is also important to measure the ratio of the total energy to the potential energy

$$E/E_{\rm pot} = \frac{\sum_i |\mathbf{B}_i|^2}{\sum_i |(\mathbf{B}_{\rm pot})_i|^2} \quad (23)$$

to study the free energy budget for a realistic coronal field.

We also calculate another four metrics to measure the force-freeness and divergence-freeness of the results. They are the current-weighted sine metric CWsin

$$\text{CWsin} \equiv \frac{\sum_i |\mathbf{J}_i|\sigma_i}{\sum_i |\mathbf{J}_i|}; \; \sigma_i = \frac{|\mathbf{J}_i \times \mathbf{B}_i|}{|\mathbf{J}_i||\mathbf{B}_i|}, \quad (24)$$

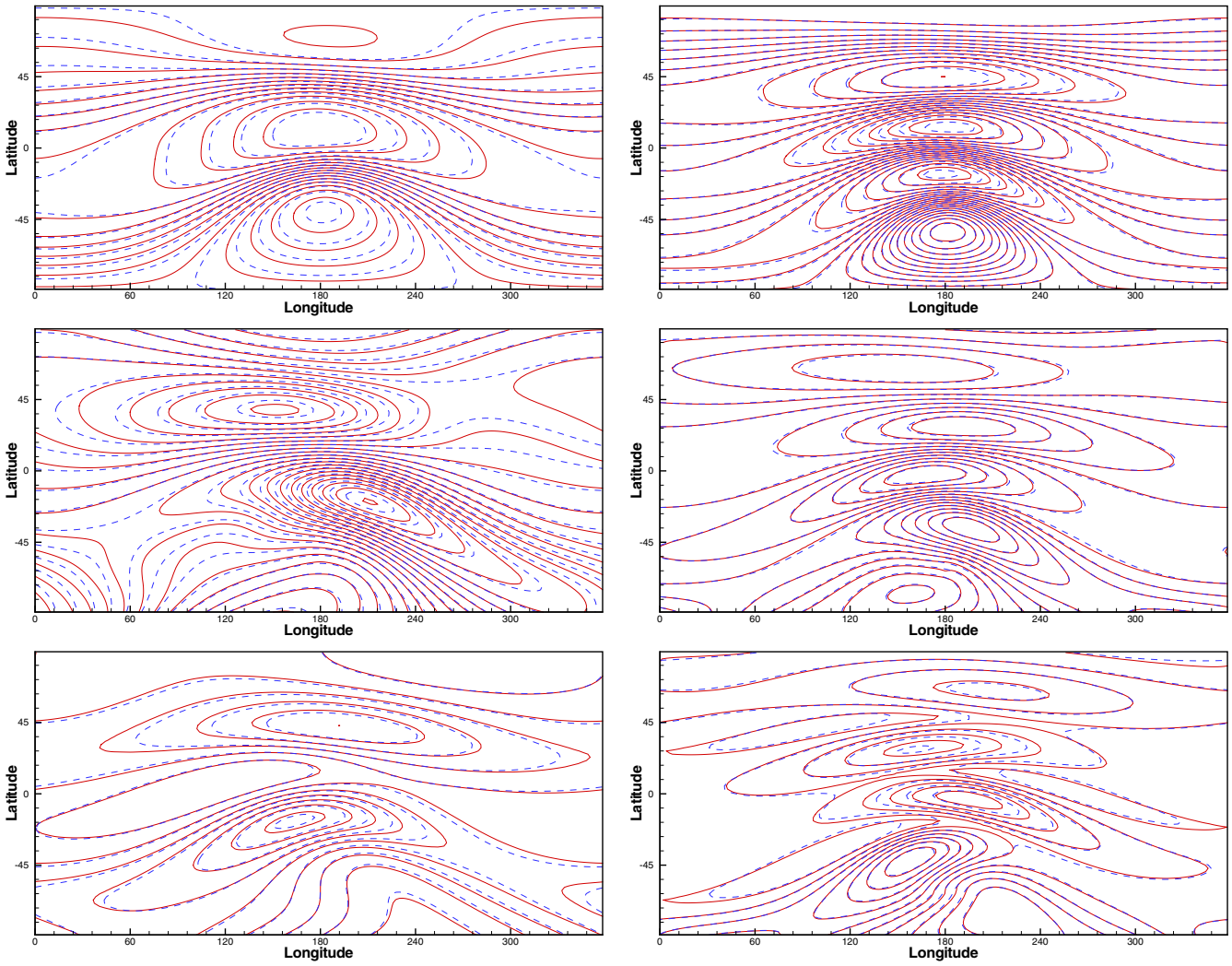

Figure 7. Contour map comparison of Low & Lou's solution (solid lines) and extrapolation solution (dashed lines) at $r = 1.5\ R_S$ for B_r (top), B_θ (middle), and B_ϕ (bottom). The left column is for CASE LL1 and the right one is for CASE LL2.

(A color version of this figure is available in the online journal.)

the divergence metric $\langle |f_i| \rangle$

$$\langle |f_i| \rangle = \frac{1}{M} \sum_i \frac{(\nabla \cdot \mathbf{B})_i}{6|\mathbf{B}_i|/\Delta x}, \tag{25}$$

and the $E_{\nabla \cdot \mathbf{B}}$ and $E_{\nabla \times \mathbf{B}}$

$$E_{\nabla \cdot \mathbf{B}} = \frac{1}{M} \sum_i \frac{|\mathbf{B}_i (\nabla \cdot \mathbf{B})_i|}{|\nabla (|\mathbf{B}|^2/2)_i|};$$
$$E_{\nabla \times \mathbf{B}} = \frac{1}{M} \sum_i \frac{|\mathbf{J}_i \times \mathbf{B}_i|}{|\nabla (|\mathbf{B}|^2/2)_i|}. \tag{26}$$

All the above metrics have been described in detail in our previous work (Jiang & Feng 2012a) and thus will not be repeated here.

4.1. Qualitative Comparison

In Figures 5 and 6, we present side-by-side comparisons of the extrapolation results with the Low & Lou models and the potential fields by plotting the 3D field configurations. For each case, the field lines are traced from the same set of foot points on the photosphere. A good agreement between our extrapolation results and the original Low & Lou solutions can be seen from the high similarity of most of the field lines. The basic difference between the extrapolated fields and the potential fields is the shearing, which is reconstructed by the bottom-boundary-driving process exerted on the initial unsheared potential fields. By placing the outer boundary far enough away, we can make most of the field lines move freely in the volume, which is helpful for the relaxation of the field lines. Figure 7 compares the field values of the $r = 1.5\ R_S$ surface by plotting the contours of the reference solutions (solid lines) and the extrapolation (dashed lines) on the same figure. As can be seen, contour lines of the fields from the reference solution and the extrapolation almost overlap with each other.

4.2. Quantitative Comparison

Quantitative metrics shown in Tables 1 and 2 demonstrate good performance of the code. In these tables, we present results of the full sphere with $r \in [1, 2]R_S$ and the lower region $r \in [1, 1.5]R_S$. For both cases, results of the vector correlation $C_{\rm vec}$ and $C_{\rm CS}$ are extremely close to the reference values, showing a perfect matching of the vector direction.

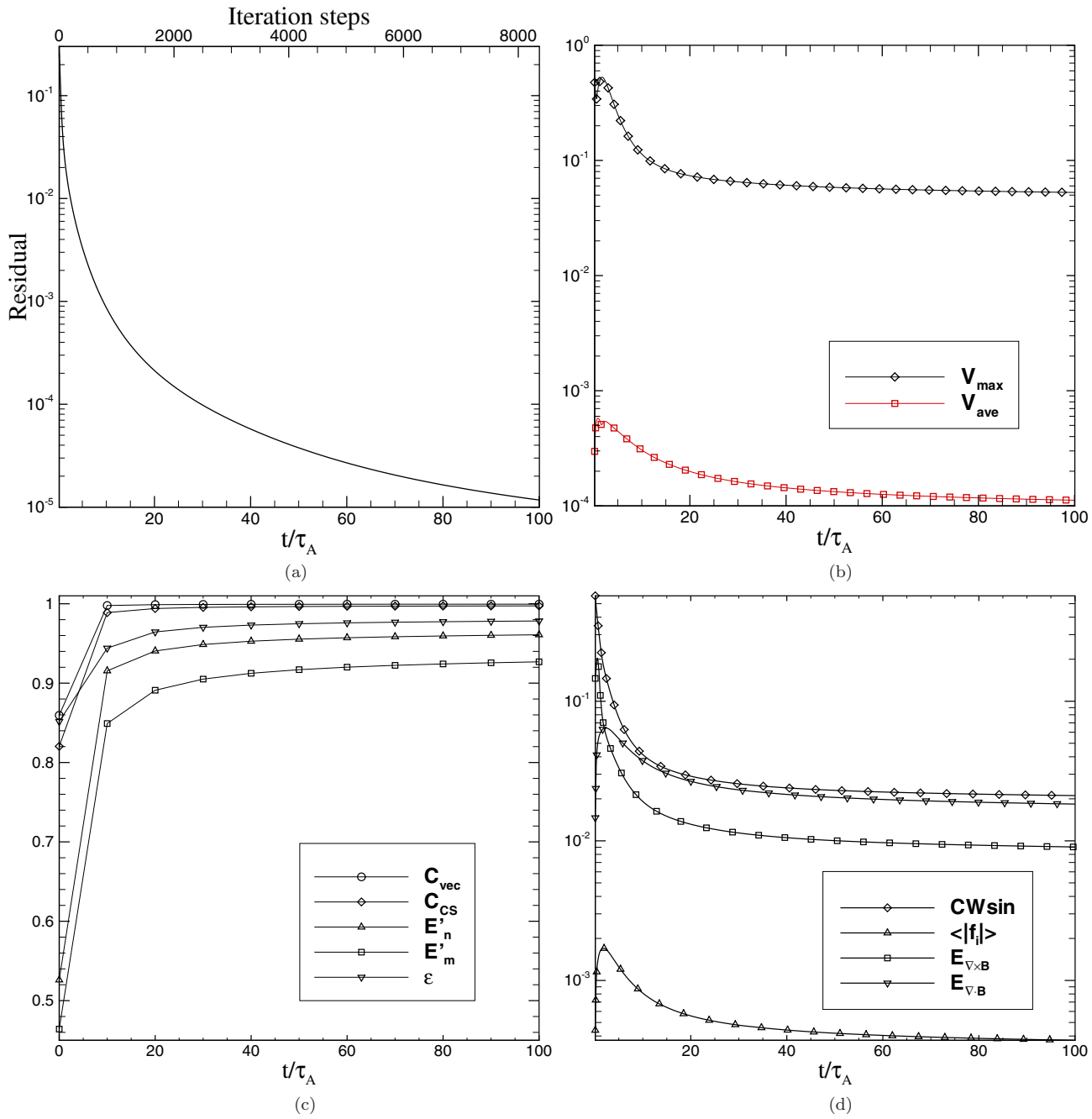

Figure 8. CASE LL1: the history of the relaxation to force-free equilibrium. (a) Evolution of residual res($\mathbf{B}_1$) with time (and the iteration steps); (b) evolution of the maximum and average velocity; and (c) and (d) evolution of the metrics.

(A color version of this figure is available in the online journal.)

Table 1
CASE LL1: Results of the Metrics

Model	$C_{\rm vec}$	$C_{\rm CS}$	$E'_{\rm n}$	$E'_{\rm m}$	ϵ	$E/E_{\rm pot}$
For $r \in [1, 2]R_S$						
Low	1	1	1	1	1	1.1741
Extrapolation	0.9995	0.9974	0.9609	0.9269	0.9783	1.1486
Potential	0.8595	0.8204	0.5261	0.4641	0.8517	1
For $r \in [1, 1.5]R_S$						
Low	1	1	1	1	1	1.1390
Extrapolation	0.9998	0.9995	0.9772	0.9668	0.9851	1.1220
Potential	0.8620	0.8236	0.5441	0.5013	0.8780	1

Table 2
CASE LL2: Results of the Metrics

Model	$C_{\rm vec}$	$C_{\rm CS}$	$E'_{\rm n}$	$E'_{\rm m}$	ϵ	$E/E_{\rm pot}$
For $r \in [1, 2]R_S$						
Low	1	1	1	1	1	1.1042
Extrapolation	0.9999	0.9965	0.9807	0.9456	1.0061	1.1110
Potential	0.9049	0.8013	0.5733	0.4515	0.9056	1
For $r \in [1, 1.5]R_S$						
Low	1	1	1	1	1	1.0999
Extrapolation	0.9999	0.9997	0.9864	0.9810	1.0063	1.1068
Potential	0.9055	0.8529	0.5861	0.5174	0.9092	1

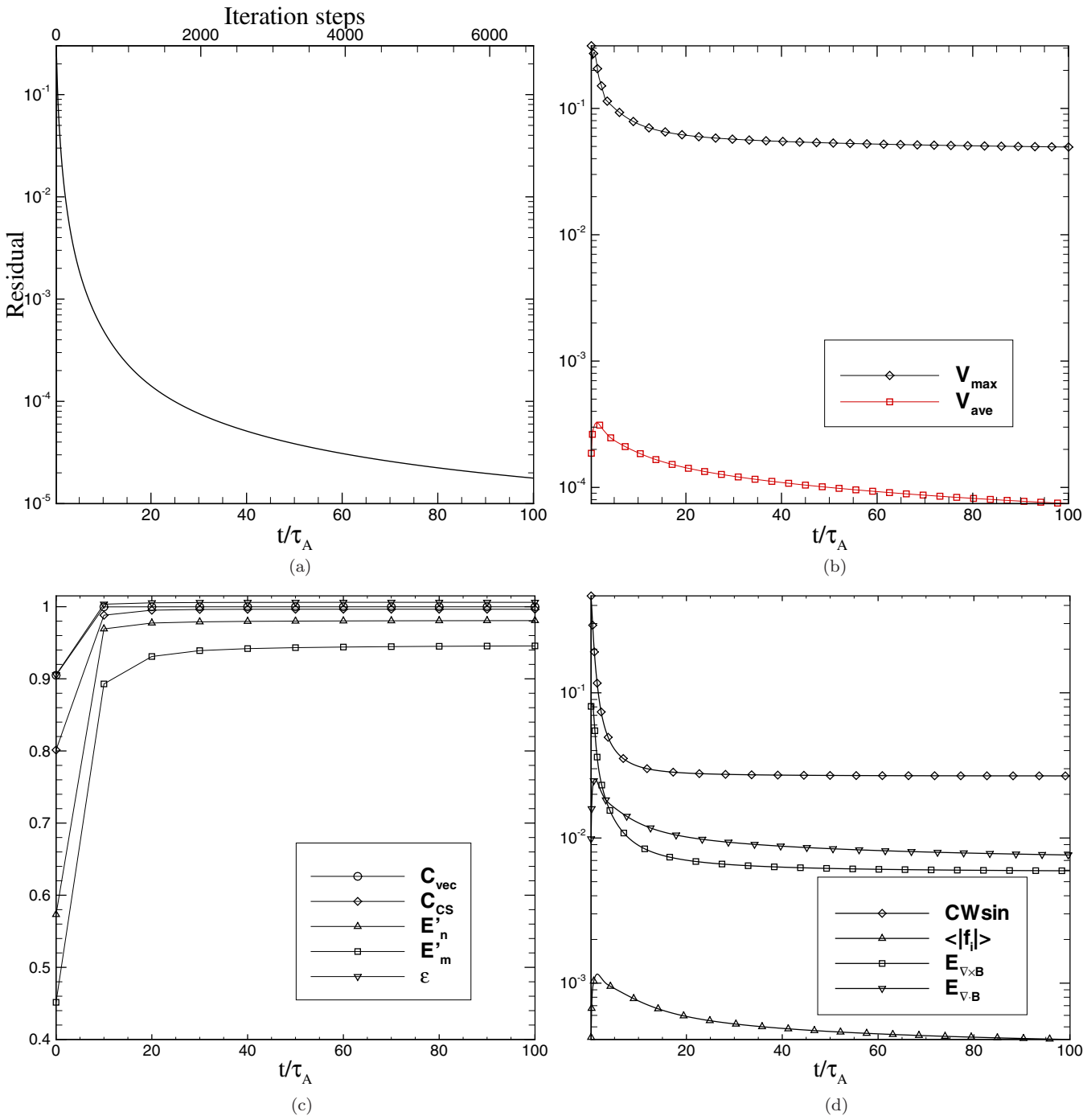

Figure 9. Same as Figure 8 but for CASE LL2.
(A color version of this figure is available in the online journal.)

Results of vector error E'_n and E'_m also score close to 1 (even the error of the most sensitive metric E'_m is smaller than 10%), while the potential solutions have results of only ∼0.5. This is very encouraging, since in previously reported tests of the Cartesian or spherical NLFFF extrapolation code with only the photospheric boundary provided, e.g., those done by Schrijver et al. (2006), Valori et al. (2007), Wiegelmann (2007), and Tadesse et al. (2009), results with $E'_m > 0.9$ are rarely achieved. These two metrics show that the original solutions are reconstructed with very high accuracy. Finally, the energy content of the non-potential fields, a critical parameter from the extrapolation used to calculate the energy budget in solar eruptions, is also well reproduced (with errors under several per cent). By comparison of the metrics, we find that accuracy of the lower region is even higher than in the full region, which means the strong fields are extrapolated better than the upper region weak fields. In real solar fields, only the lower part of the corona is close to force-free, while the upper corona is not more force-free because of the expansion of hot plasma (Gary 2001). Thus, extrapolating the lower region fields closer to the original force-free solution than the upper region fields is consistent with the real solar conditions.

Table 3 gives the metrics measuring force-freeness and divergence-freeness of the fields, which are rather small and

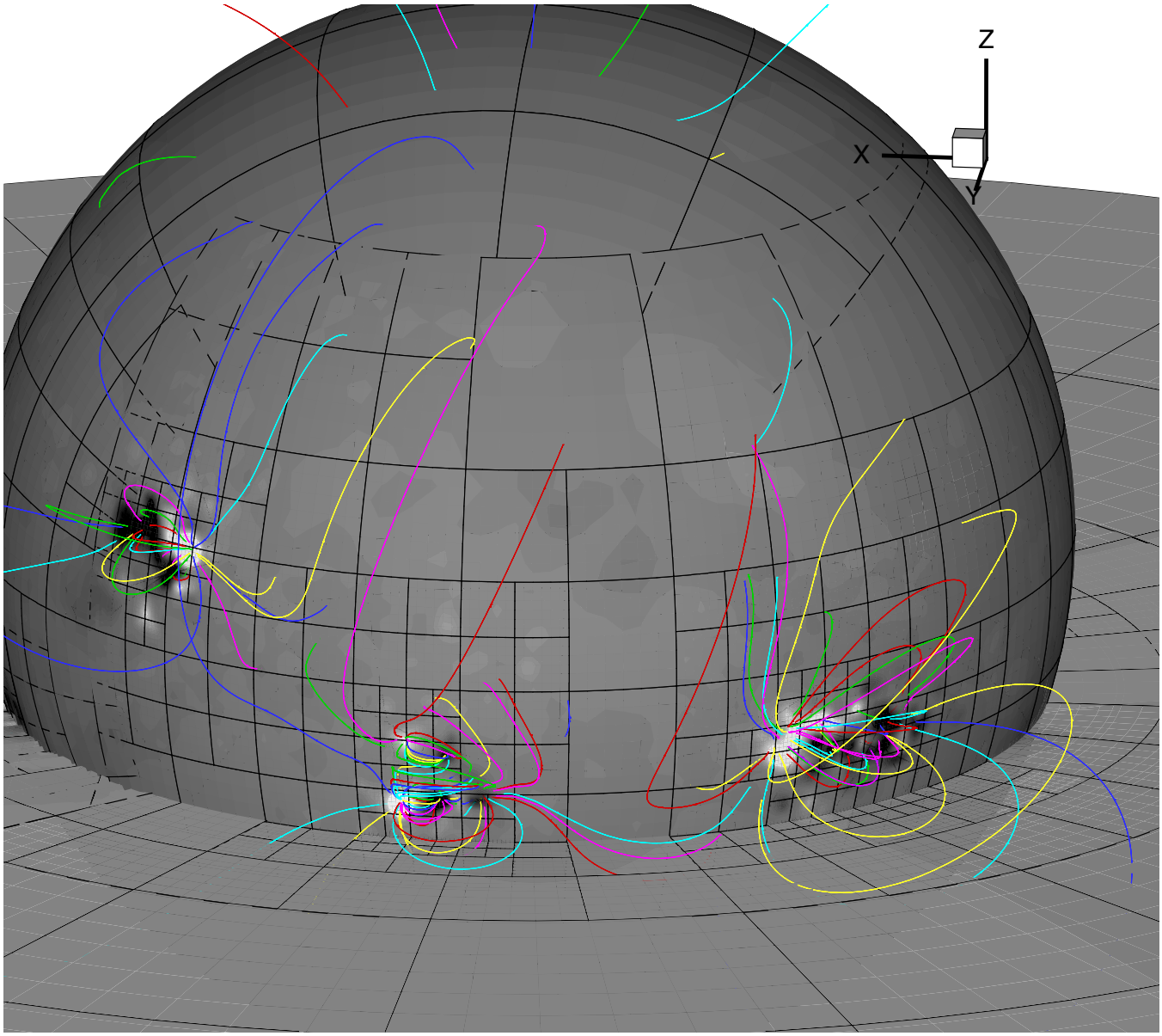

Figure 10. Example of global extrapolation with the AMR grid. The sphere represents the photosphere with grid structure outlined by the black lines (note that here each mesh cell represents one grid block). The color lines represent the magnetic field lines and the gray image represents the radial field B_r. A slice of $z = -0.3$ is plotted to show the radial mesh structure. Note that the high-resolution blocks are clustered around the active regions.

(A color version of this figure is available in the online journal.)

Table 3
Results for the Metrics Measuring Force-freeness and Divergence-freeness

Case	CWsin	$\langle \lvert f_i \rvert \rangle$	$E_{\nabla\times\mathbf{B}}$	$E_{\nabla\cdot\mathbf{B}}$
LL1	2.11×10^{-2}	3.73×10^{-4}	9.04×10^{-3}	1.83×10^{-2}
LL2	2.68×10^{-2}	4.09×10^{-4}	5.94×10^{-3}	7.64×10^{-3}

close to the level of discretization error. Unlike the first two metrics (CWsin and $\langle \lvert f_i \rvert \rangle$), which mainly characterize the geometric properties of the field, metrics $E_{\nabla\times\mathbf{B}}$ and $E_{\nabla\cdot\mathbf{B}}$ are introduced to measure the physical effect of the residual divergence and Lorentz forces on the system in the actual numerical computation (Jiang & Feng 2012a). This is important when checking the NLFFF solution if it is used to initiate any full MHD simulations. Of the present extrapolation results, the residual forces are less than 1% of the magnetic-pressure force.

4.3. Convergence Study

We finally give a study of convergence of the extrapolation. In Figures 8 and 9, we show how the system relaxes and reaches its final force-free equilibrium by plotting the temporal evolution of several parameters, including the residual of field $\mathbf{B}_1$

$$\mathrm{res}^n(\mathbf{B}_1) = \sqrt{\frac{1}{3}\sum_{\delta=x,y,z}\frac{\sum_i \left(B^n_{i\delta} - B^{n-8}_{i\delta}\right)^2}{\sum_i \left(B^n_{i\delta}\right)^2}} \qquad (27)$$

(where n denotes the iteration steps[2]), the maximum and average velocity, and the nine metrics described above. The system

[2] In the present experiments, we record the parameters not every time step but every eight steps to save the total computing time, thus $n - 8$ means the residual is for the full eight steps.

converged very quickly from an initial residual of $>10^{-1}$ to value $\sim 10^{-5}$ with time of $100\tau_A$ (about 6000 $\sim$ 8000 iteration steps; see panels (a) of the figures). The evolution of the plasma velocity indicates that initially (1) the system is driven away from the starting $\mathbf{v} = 0$ state and then (2) by the relaxation process, a static equilibrium is reached as expected with a rather small residual velocity which is only on the order of the numerical error $O(\Delta x^2)$ of the CESE solver. All the metrics plotted in the figures converged after $40\tau_A$ (less than 2000 iteration steps), when the residual is on the order of 10^{-4}, and the convergence speed of CASE LL2 is even faster than that of CASE LL1. Note that the metrics $\langle |f_i| \rangle$ and $E_{\nabla \cdot \mathbf{B}}$, like the plasma velocity, first climb to a relatively high level (see panel (d)) and then drop to the level of discretization errors. In principle, the divergence-free constraint of **B** should be fulfilled throughout the evolution, at least close to the level of the discretization error. However, an ideally dissipationless induction equation, Equation (1), with divergence-free constraint can preserve the magnetic connectivity, which makes the topology of the magnetic field unchangeable (Wiegelmann 2008) unless a finite resistivity is included to allow the reconnection and changing of the magnetic topology (Roumeliotis 1996). In the present implementation in which no resistivity is included in the induction equation, allowing high values in $\nabla \cdot \mathbf{B}$ in the initial evolution process (indicated by the climb of metric $\langle |f_i| \rangle$) may provide some freedom for changes in the magnetic topology (also note that a numerical diffusion can help topology adjustment).

Besides the extrapolation accuracy, the computing time also matters for a practical use of the NLFFF code. In the present tests, the size of the Yin–Yang grid is equivalent to $80 \times 90 \times 180$ in an ordinary spherical grid. The computation is completed in less than 2 hr using 32 processors of Intel Xeon CPU E5450 (3.00GHz). In practical applications, the computing time can be further reduced considering that it is not necessary to evolve the system to $100\tau_A$.

5. CONCLUSIONS

In this work, we present a new code for NLFFF extrapolation of the global corona. The method is implemented by installing the previous code CESE–MHD–NLFFF in the Cartesian geometry onto a Yin–Yang spherical grid. By this grid system, we can incorporate intrinsically the full-sphere computation and avoid totally the problems involved with the spherical poles. The boundary conditions are only specified on the bottom sphere and are free of any lateral-boundary information. We have examined the performance of this newly developed code using two test cases of the classic semi-analytic force-free fields by Low & Lou (1990). We show that the code runs fast and achieves good accuracy with the extrapolation solution very close to the reference field and the force-freeness and divergence-freeness constraints well fulfilled.

We note that the success of extrapolating the model solutions (i.e., the ideal force-free test cases) does not necessarily indicate successful application to the real solar data, which contain various inconsistencies and uncertainties. A practical solution to this issue may be attributed to some preprocessing methods as developed by Wiegelmann et al. (2006) and Fuhrmann et al. (2007), or to a more realistic MHD model focused on the photosphere–chromosphere interface with atmosphere stratification. For another important issue, reconstruction that needs to be performed with a much larger field of view (to more entirely characterize the currents between ARs and high over the AR) and with a higher spatial resolution (to capture the fine critical structures such as magnetic null point) is severely limited by the computational capability. Application with a grid of about 500^3 pixels is almost the upper limit for the computational capability of most recently developed or updated codes. This is rather unsatisfied if considering extrapolation with the 4096×4096 *SDO*/HMI magnetograms. Combining the global extrapolation code with the AMR, according to the intrinsic characteristics of the solar magnetic field in which the ARs represent only a small fraction of the whole surface, appears to be a promising way to resolve this issue. By the AMR technique, one can focus on the local corona, e.g., some ARs in the context of global extrapolation with the corresponding high-resolution vector magnetograms embedded in a low-resolution global vector or LoS map, as exemplified by Figure 10. In this figure,[3] mesh for the ARs is refined with three more grid levels than the background full-sphere grid (a block-AMR algorithm (Powell et al. 1999) is used, and the ratio of resolutions between the grid levels is 2). The grid structure can be dynamically adjusted during the MHD-relaxation process to capture the strong currents and important magnetic structures (e.g., flux ropes) by carefully designing the AMR refinement criteria. Our future work will include performing more stringent testing of the code and installation of the code on an AMR grid for practical application to *SDO*/HMI data.

The work is jointly supported by the 973 program under grant 2012CB825601, the Chinese Academy of Sciences (KZZD-EW-01-4), National Natural Science Foundation of China (41031066, 40921063, 40890162, and 41074122), and the Specialized Research Fund for State Key Laboratories.

REFERENCES

Aly, J. J. 1989, Sol. Phys., 120, 19
Amari, T., Aly, J. J., Luciani, J. F., Boulmezaoud, T. Z., & Mikic, Z. 1997, Sol. Phys., 174, 129
Amari, T., Boulmezaoud, T. Z., & Aly, J. J. 2006, A&A, 446, 691
Bobra, M. G., van Ballegooijen, A. A., & DeLuca, E. E. 2008, ApJ, 672, 1209
Contopoulos, I., Kalapotharakos, C., & Georgoulis, M. K. 2011, Sol. Phys., 269, 351
DeRosa, M. L., Schrijver, C. J., Barnes, G., et al. 2009, ApJ, 696, 1780
Feng, X., Zhou, Y., & Wu, S. T. 2007, ApJ, 655, 1110
Feng, X. S., Yang, L. P., Xiang, C. Q., et al. 2012, Sol. Phys., 279, 207
Feng, X. S., Yang, L. P., Xiang, C. Q., et al. 2010, ApJ, 723, 300
Fuhrmann, M., Seehafer, N., & Valori, G. 2007, A&A, 476, 349
Gary, D. E., & Hurford, G. J. 1994, ApJ, 420, 903
Gary, G. A. 2001, Sol. Phys., 203, 71
He, H., & Wang, H. 2006, MNRAS, 369, 207
He, H., & Wang, H. 2008, J. Geophys. Res., 113, 5
Henshaw, W. D., & Schwendeman, D. W. 2008, J. Comput. Phys., 227, 7469
Isaacson, E., & Keller, H. B. 1966, Analysis of Numerical Methods (New York: Wiley)
Jiang, C., & Feng, X. 2012a, ApJ, 749, 135
Jiang, C., Feng, X., Fan, Y., & Xiang, C. 2011, ApJ, 727, 101
Jiang, C. W., & Feng, X. S. 2012b, Sol. Phys., in press
Jiang, C. W., Feng, X. S., Zhang, J., & Zhong, D. K. 2010, Sol. Phys., 267, 463
Kageyama, A., & Sato, T. 2004, Geochem. Geophys. Geosyst., 5, 9005
Lin, H., Kuhn, J. R., & Coulter, R. 2004, ApJ, 613, L177
Low, B. C., & Lou, Y. Q. 1990, ApJ, 352, 343
McClymont, A. N., Jiao, L., & Mikic, Z. 1997, Sol. Phys., 174, 191
Metcalf, T. R., DeRosa, M. L., Schrijver, C. J., et al. 2008, Sol. Phys., 247, 269

[3] This figure is not for a real NLFFF result but rather an extrapolation of the potential field based on the synoptic LoS map of solar Carrington rotation 2029 obtained from *SOHO*/MDI. It is plotted as an outlook for our future work using *SDO*/HMI data, since we have not obtained the full-disk vector magnetogram from *SDO*/HMI.

Nakamizo, A., Tanaka, T., Kubo, Y., et al. 2009, J. Geophys. Res., 114, A07109
Powell, K. G., Roe, P. L., Linde, T. J., Gombosi, T. I., & de Zeeuw, D. L. 1999, J. Comput. Phys., 154, 284
Priest, E. R., & Forbes, T. G. 2002, A&AR, 10, 313
Roumeliotis, G. 1996, ApJ, 473, 1095
Sakurai, T. 1989, Space Sci. Rev., 51, 11
Savcheva, A., & van Ballegooijen, A. 2009, ApJ, 703, 1766
Schrijver, C. J., De Rosa, M. L., Metcalf, T. R., et al. 2006, Sol. Phys., 235, 161
Solanki, S. K., Inhester, B., & Schüssler, M. 2006, Rep. Prog. Phys., 69, 563
Su, Y., van Ballegooijen, A., Lites, B. W., et al. 2009a, ApJ, 691, 105
Su, Y., van Ballegooijen, A., Schmieder, B., et al. 2009b, ApJ, 704, 341
Tadesse, T. 2011, PhD thesis, Max Planck Institute for Solar System Research
Tadesse, T., Wiegelmann, T., & Inhester, B. 2009, A&A, 508, 421
Tadesse, T., Wiegelmann, T., Inhester, B., & Pevtsov, A. 2011, A&A, 527, A30
Tadesse, T., Wiegelmann, T., Inhester, B., & Pevtsov, A. 2012, Sol. Phys., 277, 119
Tanaka, T. 1994, J. Comput. Phys., 111, 381
Usmanov, A. V. 1996, in AIP Conf. Ser. 382, A Global 3-D MHD Solar Wind Model with Alfvén Waves, ed. D. Winterhalter et al. (Melville, NY: AIP), 141
Valori, G., Kliem, B., & Fuhrmann, M. 2007, Sol. Phys., 245, 263
van Ballegooijen, A. A. 2004, ApJ, 612, 519
Wang, H., Chae, J., Yurchyshyn, V., et al. 2001, ApJ, 559, 1171
Wheatland, M. S., Sturrock, P. A., & Roumeliotis, G. 2000, ApJ, 540, 1150
Wiegelmann, T. 2007, Sol. Phys., 240, 227
Wiegelmann, T. 2008, J. Geophys. Res., 113, 3
Wiegelmann, T., Inhester, B., & Sakurai, T. 2006, Sol. Phys., 233, 215
Yan, Y., & Li, Z. 2006, ApJ, 638, 1162